SUPPLEMMENTARY INFORMATION

An air-stable high-performance single-molecule magnet operating as a luminescent thermometer below its blocking temperature

Julio Corredoira-Vázquez,[abc] Cristina González-Barreira,[a] Matilde Fondo,*[a] Ana M. García Deibe,[a] Jesús Sanmartín-Matalobos,[ab] Silvia Gómez-Coca,[d] Eliseo Ruiz,[d] Carlos D. S. Brites,[d] Luís D. Carlos*[c]

[a] Departamento de Química Inorgánica, Facultade de Química, Universidade de Santiago de Compostela, 15782 Santiago de Compostela, Spain.
[b] Phantom-g, CICECO – Aveiro Institute of Materials, Department of Physics, University of Aveiro, 3810-193 – Aveiro, Portugal.
[c] Institute of Materials (iMATUS), Universidade de Santiago de Compostela, 15782 Santiago de Compostela, Spain.
[d] Departament de Química Inorgànica i Orgànica and Institut de Recerca de Química Teòrica i Computacional Universitat de Barcelona Diagonal 645, 08028 Barcelona, Spain.

Corresponding authors: matilde.fondo@usc.es and lcarlos@ua.pt

Contents

1. Experimental section

Materials and general methods

All chemical reagents were purchased from commercial sources and used as received without further purification. Elemental analyses of C, H and N were performed on a Themoscientific Flash Smart analyser. FT-IR spectra were recorded on a Varian FT-IR 670 spectrometer equipped with an attenuated total reflectance (ATR) attachment, in the 500-4000 cm^{-1} range. ^{1}H NMR spectra of the diamagnetic yttrium complexes were recorded on a Agilent VNMRS-300 spectrometer.

Syntheses

$\{[Dy(L^{N6en})(OSiPh_3)_2](BPh_4)\}\cdot 1.5CH_2Cl_2$ (**1**$\cdot 1.5CH_2Cl_2$) was obtained from the previously reported precursor $\{[Dy(L^{N6en})(CH_3COO)_2](NO_3)\}\cdot 2H_2O$,[1] as follows: triphenylsilanol (98%, 0.077 g, 0.274 mmol) and sodium hydride (60% in a mineral oil dispersion, 0.011 g, 0.274 mmol) were dissolved in dry tetrahydrofuran (5 mL) under an argon atmosphere, and stirred for 4 h. Simultaneously, $\{[Dy(L^{N6en})(CH_3COO)_2](NO_3)\}\cdot 2H_2O$ (0.095 g, 0.137 mmol) was dissolved in methanol (10 mL) and sodium tetraphenylborate (99.5%, 0.047 g, 0.137 mmol) was added to this solution, giving a yellow suspension, which was stirred for 4 h and then concentrated to dryness, giving a yellow solid. Next, the solution of sodium triphenylsilanolate was added over this solid under an argon atmosphere and stirred for 16 h, giving a suspension, which was centrifugated. The supernatant was decanted, and the white solid was dried in the lab stove. Recrystallization of this solid in dichloromethane by diffusion with diethyl ether at ~5˚C led to the isolation of $\{[Dy(L^{N6en})(OSiPh_3)_2](BPh_4)\}\cdot 1.5CH_2Cl_2$ as colourless crystals. Yield: 0.062 g (33%). Elemental analysis calcd. for $C_{79.5}H_{71}BCl_3DyN_6O_2Si_2$ (1478.29): C 64.53, N 5.68, H 4.80 %. Found: C 64.35, N 5.65, H 4.88%. IR (ATR, $\tilde{\nu}$/cm^{-1}): 1592 (C=N$_{py}$), 1662 (C=N$_{imine}$).

$\{[Y(L^{N6en})(CH_3COO)_2](BPh_4)\}\cdot H_2O$ (**2**$\cdot H_2O$): 2,6-pyridinedicarboxaldehyde (0.100 g, 0.740 mmol) was dissolved in dry methanol (30 mL). Then, yttrium acetate tetrahydrate (99.9%, 0.125 g, 0.370 mmol) and ethylenediamine (99%, 0.053 mL, 0.777 mmol) were added. The reaction was refluxed for 24 hours, giving a yellow solution. To this solution sodium tetraphenylborate (99%, 0.128 g, 0.370 mmol) was added, and the resultant yellow suspension was stirred for 2 h 30 min. Removing the solvent under vacuum produced a yellow solid, which was washed with distilled water (100 mL) and centrifugated. The supernatant was decanted, and the yellow solid was dried in the stove. Yield: 0.258 g (81%). Elemental analysis calcd. for $C_{46}H_{46}BYN_6O_5$ (862.58): C 64.05, N 9.74, H 5.38%. Found: C 63.90, N 9.84, H 5.30 %. IR (ATR, $\tilde{\nu}$/cm^{-1}): 1540 (C=O$_{OAc}$), 1590 (C=N$_{py}$), 1660 (C=N$_{imine}$), 3055 (OH). ^{1}H NMR (300 MHz, DMSO-d$_6$/ppm): 1.44 (s, 6H, CH$_3$ acetate); 3.94 (s, 8H, H4); 6.79 (t, 4H, BPh$_4$); 6.90-6.94 (m, 8H, BPh$_4$); 7.15-7.21 (m, 8H, BPh$_4$); 8.06 (d, 4H, H2); 8.35 (t, 2H, H1); 8.83 (s, 4H, H3).

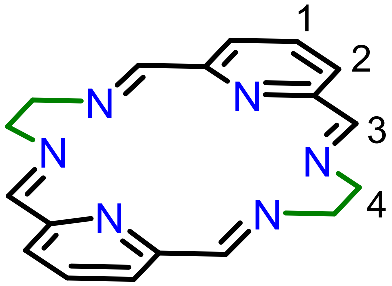

Macrocyclic ligand in the complexes, with numbering scheme for ^{1}H NMR.

{[Y(L^{N6en})($OSiPh_3$)$_2$](BPh_4)}·$3H_2O$ (**3**·$3H_2O$): triphenylsilanol (98%, 0.067 g, 0.237 mmol) and sodium hydride (60% in a mineral oil dispersion, 0.009 g, 0.237 mmol) were dissolved in dry tetrahydrofuran (6 mL) under an argon atmosphere and stirred for 20 min. Then, this solution was added over **2**·H_2O (0.102 g, 0.118 mmol) under argon and stirred for 17 h, giving a suspension. The pale-yellow solid was separated by centrifugation and dried in the stove. Yield: 0.082 g (52 %). Elemental analysis calcd. for $C_{78}H_{74}BYN_6O_5Si_2$ (1331.30): C 70.37, N 6.31, H 5.60%. Found: C 70.54, N 6.79, H 5.50%. IR (ATR, $\tilde{\nu}$/cm^{-1}): 1594 (C=N$_{py}$), 1664 (C=N$_{imine}$), 3051 (OH). ^{1}H NMR (500 MHz, DMSO-d$_6$/ppm): 3.71 (s, 8H, H4); 6.77-6.82 (m, 6H); 6.91-6.96 (m, 12H); 6.99-7.13 (m, 16H); 7.15-7.30 (m, 16H, BPh_4 + $2Ph_3SiO$); 8.08 (d, 4H, H2); 8.45 (t, 2H, H1); 8.83 (s, 4H, H3). For labelling, see Scheme above.

{[$Dy_{0.1}Y_{0.9}$(L^{N6en})($OSiPh_3$)$_2$](BPh_4)}·$1.5CH_2Cl_2$ (**1@Y**·$1.5CH_2Cl_2$): **1**·$1.5CH_2Cl_2$ (0.008 g, 5.41x10^{-3} mmol) and **3**·$3H_2O$ (0.076 g, 5.71x10^{-2} mmol) were dissolved in dichloromethane (50 mL). The solution was stirred for 24 h at room temperature. Then, the solvent was removed under vacuum, giving a pale yellow solid, which was dried in the stove. Yield: 0.069 g (93 %). Elemental analysis calcd. for $C_{79.5}H_{71}BDy_{0.1}Y_{0.9}N_6O_2Si_2Cl_3$ (1411.35): C 67.66, N 5.95, H 5.07 %. Found: C 67.53, N 6.21, H 5.18 %. IR (ATR, $\tilde{\nu}$/cm^{-1}): 1593 (C=N$_{py}$), 1663 (C=N$_{imine}$). Micro X-ray fluorescence: Dy: Y ratio 0.1: 0.9.

Crystal structure analyses

Diffraction data for single crystals of **1**·$1.5CH_2Cl_2$ were collected at 250(2) K, using monochromatised Mo–*Kα* radiation, λ = 0.71073 Å, using a Bruker D8 Venture Photon III-14 diffractometer. Data were routinely processed and corrected, including a multi–scan absorption corrections using the SADABS routine.[2] The solution of the structure was attained by standard direct methods employing SHELXT,[3] and subsequently refined with SHELXL program,[4] using a full matrix least squares on F^2. All non–hydrogen atoms were refined with anisotropic thermal parameters. Hydrogen atoms were mostly included in the structure factor calculation in geometrically idealized positions, with thermal parameters depending on the parent atom, by using a riding model. More details of the refinement, as well as crystal data are collected in Table S1.

CCDC 2262113 contains the supplementary crystallographic data for this paper. These data can be obtained free of charge from the Cambridge Crystallographic Data Centre via www.ccdc.cam.ac.uk/data_request/cif.

Powder X-ray diffraction studies

The powder diffractogram for **1**·$1.5CH_2Cl_2$ was recorded in a Philips diffractometer with a control unity type “PW1710”, a vertical goniometer type “PW1820/00” and a generator type “Enraf Nonius FR590”, operating at 40 kV and 30 mA, using monochromated Cu-Kα (λ = 1.5418 Å) radiation. A scan was performed in the range $2 < 2\theta < 30°$ with t = 3 s and $\Delta 2\theta = 0.02°$. LeBail refinement was obtained with the aid of HighScore Plus Version 3.0d.

Magnetic measurements

Magnetic *dc* measurements for **1**·$1.5CH_2Cl_2$ were carried out with a Quantum Design SQUID MPMS3 susceptometer. The *dc* magnetic susceptibility data were recorded under a magnetic field of 0.1 T in the temperature range 2–300 K. Magnetization measurements at 2.0 K were recorded under magnetic fields ranging from 0 to 5 T. Diamagnetic corrections were estimated from Pascal’s Tables. Alternating current (*ac*) susceptibility measurements at zero *dc* field were performed with an oscillating *ac* field of 3 Oe, and different *ac* frequencies depending on the temperature range (between 2 and 110 K). Thus, measurements between 2 and 60 K were recorded in a Quantum Design SQUID MPMS susceptometer at *ac* frequencies ranging from 0.1 to 1488 Hz while measurements between 60 and 110 K were registered with a PPMS Quantum Design susceptometer with *ac* frequencies in the range 50-10000 Hz. Hysteresis cycles for **1**·$1.5CH_2Cl_2$ were recorded between 2 and 18 K, and for **1@Y**·$1.5CH_2Cl_2$ between 2 and 46 K, in a Quantum Design SQUID MPMS3 susceptometer with a sweep rate of 10 mTs^{-1}. The field was corrected using a Pd reference sample measured under the same conditions. FC/ZFC measurements for both **1**·$1.5CH_2Cl_2$ and **1@Y**·$1.5CH_2Cl_2$ were registered in a Quantum Design SQUID MPMS3 susceptometer under a magnetic field of 2000 Oe and with a sweep rate of 2 Kmin^{-1}.

Luminescence measurements

The solid state temperature-dependent emission and excitation spectra of **1**·1.5CH_2Cl_2 and **1@Y**·1.5CH_2Cl_2 were acquired in a Fluorolog3® spectrofluorometer (FL3-2T, Horiba) with a modular double grating excitation monochromator (fitted with a 1200 grooves per mm grating blazed at 330 nm) and a TRIAX 320 single emission monochromator (fitted with a 1200 grooves per mm grating blazed at 500 nm, reciprocal linear density of 2.6 nm mm^{-1}), coupled with a photomultiplier (R298, Hamamatsu), using the front face acquisition mode. The excitation source was a 450 W Xe arc lamp. The emission spectra were corrected for detection and the optical spectral response of the spectrofluorimeter, and the excitation spectra were corrected for the spectral distribution of the lamp intensity using a photodiode reference detector. The temperature was controlled using a helium-closed cycle cryostat, a vacuum system (4×10^{-4} Pa), and an autotuning temperature controller (Lakeshore 330, Lakeshore) with a resistance heater. The temperature was measured using a silicon diode cryogenic sensor (DT-470-SD, Lakeshore) with accuracies of ±0.5 K (12–30 K), ±0.25 K (30–60 K), and ±0.15 K (60–340 K).

2. Structural characterization

Table S1. Crystal data and structure refinement for **1**·1.5CH$_2$Cl$_2$.

	1·1.5CH$_2$Cl$_2$
Empirical formula	$C_{79.5}H_{71}BCl_3DyN_6O_2Si_2$
Formula weight	1478.26
Temperature	250(2) K
Wavelength	0.71073 Å
Crystal system	Triclinic
Space group	*P*-1
a	14.737(4) Å
b	15.531(4) Å
c	16.782(4) Å
α	93.188(9)°
β	98.299(9)°
γ	104.492(9)°
Volume	3662.9(17) Å^3
Z	2
Absorption coefficient	1.212 mm^{-1}
F(000)	1512
Crystal size	0.18 x 0.17 x 0.06 mm^3
Theta range for data collection	2.464 to 27.484 °
Reflections collected	205931
Independent reflections	16756 (R_{int} = 0.0675)
Completeness to theta = 25.242°	99.8 %
Refinement method	Full-matrix least-squares on F^2
Data / restraints / parameters	16756 / 2 / 944
Goodness-of-fit on F^2	1.083
Final R indices [I>2sigma(I)]	R_1 = 0.0354, wR_2 = 0.1006
R indices (all data)	R_1 = 0.0492, wR_2 = 0.1119

Table S2. Some selected structural and magnetic parameters for hbp Dy^{3+} complexes with N_6 macrocycles and triphenylsilanolate as auxiliary ligand.

Metal complex	ChSM[a]	Dy-N	Dy-O	Dev. N-plane[b]	Dev. Dy-plane[c]	α(O-Dy-O)	θ(planes)[d]	Plane subst.[e]	U_{eff} (K)[f]	Mechanism[g]	T_B^H[h]	Ref.
$[Dy(L^{5RRRR})(Ph_3SiO)_2](BPh_4)$	1.933	2.616(4)-2.712(3)	2.123(3) 2.139(3)	0.113-0.440	0.095	178.1(1)	87.87	ED	1455	O + R + QTM	5 (3.1)	5
$[Dy(L^{5SSSS})(Ph_3SiO)_2](BPh_4)$	1.904	2.618(5)-2.710(4)	2.128(4) 2.141(3)	0.110-0.437	0.096	178.5(1)	87.74	ED	1457	O + R + QTM	5 (3.1)	
$[Dy(L^{5RRRR})(Ph_3SiO)_2][(3\text{-}Br\text{-}Ph)BPh_3]$	1.977	2.608(5)-2.720(5)	2.131(4) 2.138(4)	0.096-0.442	0.094	175.5(2)	87.46	ED	1363	O + R + QTM	4 (4)	6
$[Dy(L^{5SSSS})(Ph_3SiO)_2][(3\text{-}Br\text{-}Ph)BPh_3]$	1.964	2.597(7)-2.718(6)	2.133(5) 2.137(5)	0.095-0.441	0.092	175.0(2)	87.41	ED	1415	O + R + QTM	1.9 (4)	
$[Dy(L^{5RRRR})(Ph_3SiO)_2][(4\text{-}Br\text{-}Ph)BPh_3]$	1.897	2.618(9)-2.699(8)	2.136(7) 2.145(7)	0.116-0.441	0.101	178.4(3)	88.21	ED	1369	O + R + QTM	1.9 (4)	
$[Dy(L^{5SSSS})(Ph_3SiO)_2][(4\text{-}Br\text{-}Ph)BPh_3]$	1.909	2.623(7)-2.702(7)	2.140(6) 2.141(5)	0.116-0.435	0.105	179.1(2)	88.43	ED	1434	O + R + QTM	1.9 (4)	
$[Dy(L^{7RRRR})(Ph_3SiO)_2](PF_6)$	1.338	2.675(8)-2.744(7)	2.124(6) 2.139(7)	0.014-0.228	0.022	177.9(2)	85.66	EW	1833	O + R	n.r.	7
$[Dy(L^{7SSSS})(Ph_3SiO)_2](PF_6)$	1.332	2.664(7)-2.736(5)	2.122(6) 2.147(6)	0.007-0.221	0	178.8(2)	85.56	EW	1819	O + R	20 (20)[i]	
$[Dy(L^8)(Ph_3SiO)_2](BPh_4)$	2.163	2.6057(18)-2.635(2)	2.1425(16) 2.1514(16)	0.195-0.518	0.024	176.14(7)	88.15	ED	1124	O + R + QTM	5 (4)	8
$[Dy(L^8)(Ph_3SiO)_2](PF_6)$	2.271	2.551(6)-2.642(6)	2.153(7) 2.163(6)	0.076-0.530	0.074	179.8(3)	84.41	ED	1080	O + R + QTM	n.r.	
$[Dy(L^9)(Ph_3SiO)_2](BPh_4)$	3.908	2.139(4)-2.143(4)	2.524(7)-2.682(8)	0.144-0.784	0.031	169.06(17)	87.84	-	584	O + R + QTM	13 (20)	9
$[Dy(L^{N6en})(Ph_3SiO)_2](BPh_4)$	**1a**: 1.126 **1b**: *ca.* 1.4	2.652(3)-2.669(3) 2.516(8-2.723(9)	2.126(2) 2.140(2)	0.154-0.156 51%:0.221-0.224 49%:0.012-0.328	0 0 0.104	180 180 180	90 90 90	-	1538	O + R + QTM	40 (10)[i]	This work

n.r.: not reported; [a] according to SHAPE; [b] distance from the equatorial *N*-atoms to the mean calculated N_5 or N_6 planes in Å; [c] distance from the Dy^{3+} ions to the mean calculated N_5 or N_6 planes in Å; [d] angle between the N_5 or N_6 planes and the O-Dy-O plane; [e] character of the substituents of the imine moieties: ED: electron-donating, EW: electron-withdrawing; [f] $H_{dc} = 0$; [g] relaxation mechanism: O = Orbach, R: Raman, QTM = Quantum Tunnel; [h] in K (sweep rate, mTs^{-1}). [i] Magnetic hysteresis measurements performed on the magnetically diluted samples of Dy:Y (1:19 or 1:10).

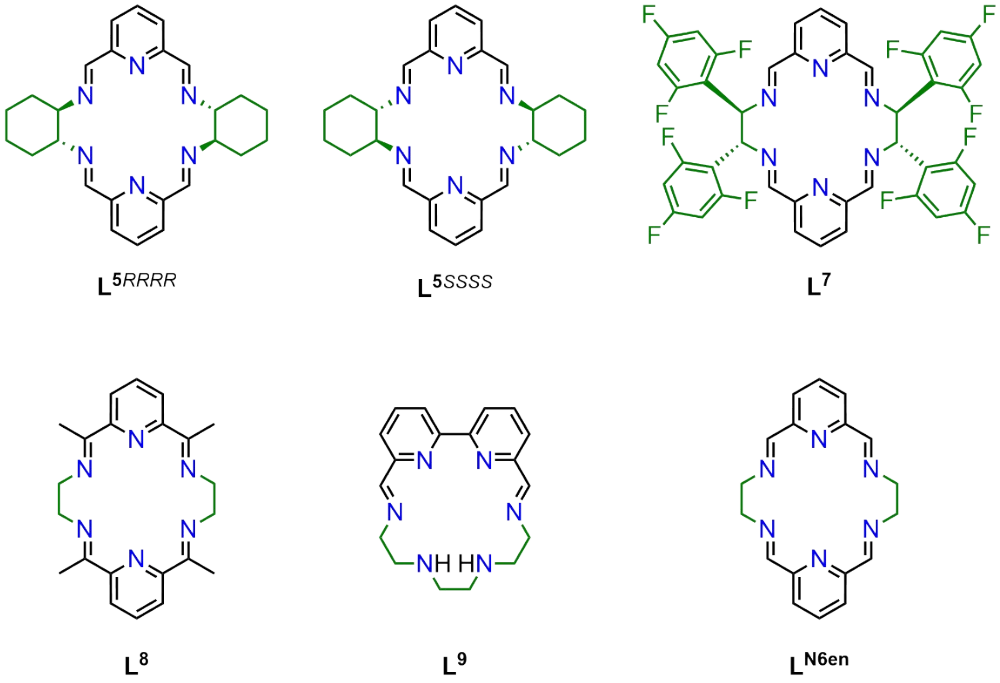

$\mathbf{L}^{5RRRR}$ $\mathbf{L}^{5SSSS}$ $\mathbf{L}^{7}$

$\mathbf{L}^{8}$ $\mathbf{L}^{9}$ $\mathbf{L}^{N6en}$

Ligands in **Table S1**. Adapted from reference.[10] Creative Commons license.

Table S3. SHAPE v2.1. Continuous Shape Measures calculation (c) 2013. Electronic Structure Group, Universitat de Barcelona.

ETBPY-8	13 D_{3h} Elongated trigonal bipyramid
TT-8	12 T_d Triakis tetrahedron
JSD-8	11 D_{2d} Snub diphenoid J84
BTPR-8	10 C_{2v} Biaugmented trigonal prism
JBTPR-8	9 C_{2v} Biaugmented trigonal prism J50
JETBPY-8	8 D_{3h} Johnson elongated triangular bipyramid J14
JGBF-8	7 D_{2d} Johnson gyrobifastigium J26
TDD-8	6 D_{2d} Triangular dodecahedron
SAPR-8	5 D_{4d} Square antiprism
CU-8	4 O_h Cube
HBPY-8	3 D_{6h} Hexagonal bipyramid
HPY-8	2 C_{7v} Heptagonal pyramid
OP-8	1 D_{8h} Octagon

1a

Structure [ML$_8$]	ETBPY-8	TT-8	JSD-8	BTPR-8	JBTPR-8	JETBPY-8	JGBF-8
	22.651,	7.808,	17.425,	16.653,	16.762,	24.384,	10.700,

TDD-8	SAPR-8	CU-8	**HBPY-8**	HPY-8	OP-8
14.290,	17.062,	6.928,	**1.126**,	21.456,	29.794

1b (51 %)

Structure [ML$_8$]	ETBPY-8	TT-8	JSD-8	BTPR-8	JBTPR-8	JETBPY-8	JGBF-8
	22.056,	6.685,	16.408,	15.638,	15.546,	23.203,	10.217,

TDD-8	SAPR-8	CU-8	**HBPY-8**	HPY-8	OP-8
13.167,	15.939,	5.794,	**1.401**,	21.701,	29.697

1b (49 %)

Structure [ML$_8$]	ETBPY-8	TT-8	JSD-8	BTPR-8	JBTPR-8	JETBPY-8	JGBF-8
	20.538,	8.995,	15.828,	15.747,	15.799,	22.215,	8.729,

TDD-8	SAPR-8	CU-8	**HBPY-8**	HPY-8	OP-8
13.985,	16.649,	8.285,	**1.438**,	20.363,	29.049

Table S4. Main bond distances (Å) and angles (°) for **1**·1.5CH_2Cl_2.

Dy1-O1	2.126(2)	Dy2-O2	2.140(2)
Dy1-O1$^{\#1}$	2.126(2)	Dy2-O2$^{\#2}$	2.140(2)
Dy1-N13	2.652(3)	Dy2-N23	2.516(8)
Dy1-N13$^{\#1}$	2.652(3)	Dy2-N23$^{\#2}$	2.516(8)
Dy1-N12	2.662(3)	Dy2-N22	2.667(3)
Dy1-N12$^{\#1}$	2.662(3)	Dy2-N22$^{\#2}$	2.667(3)
Dy1-N11	2.669(3)	Dy2-N21	2.679(8)
Dy1-N11$^{\#1}$	2.669(3)	Dy2-N21$^{\#2}$	2.679(8)
O1-Si1	1.590(2)	Dy2-N21'	2.647(8)
		Dy2-N23'	2.723(9)
		O2-Si2	1.4375(16)
O1-Dy1-O1$^{\#1}$	180.0	O2-Dy2-O2$^{\#1}$	180.0
N13$^{\#1}$-Dy1-N13	180.0	N23$^{\#1}$-Dy2-N23	180.0
N12$^{\#1}$-Dy1-N12	180.0	N22$^{\#1}$-Dy2-N22	180.0
N11$^{\#1}$-Dy1-N11	180.0	N21$^{\#1}$-Dy2-N21	180.0
O1-Dy1-N13	95.68(9)	O2-Dy2-N23	97.0(3)
O1-Dy1-N12	87.06(9)	O2-Dy2-N22	88.06(9)
O1-Dy1-N11	91.41(9)	O2-Dy2-N21	95.8(2)
		O2-Dy2-N21’	82.1(3)
		O2-Dy2-N23’	82.7(2)

Symmetry transformations used to generate equivalent atoms: $^{\#1}$ -x+2,-y+2,-z; $^{\#2}$ -x+1,-y+1,-z+1

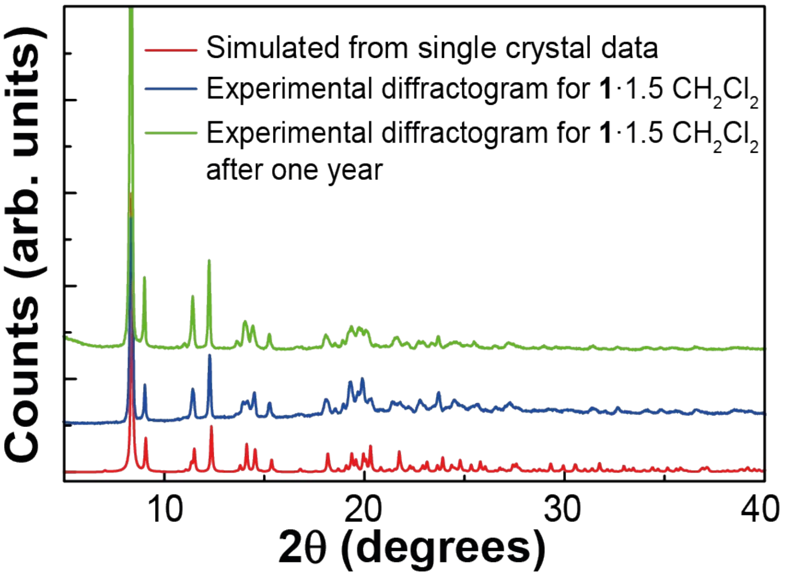

Figure S1. Comparative powder X-ray diffractograms for **1**·1.5CH_2Cl_2. Red: calculated diffractogram using the data obtained from single X-ray diffraction studies; blue: experimental diffractogram for a fresh microcrystalline sample; green: experimental diffractogram for the microcrystalline sample after one year.

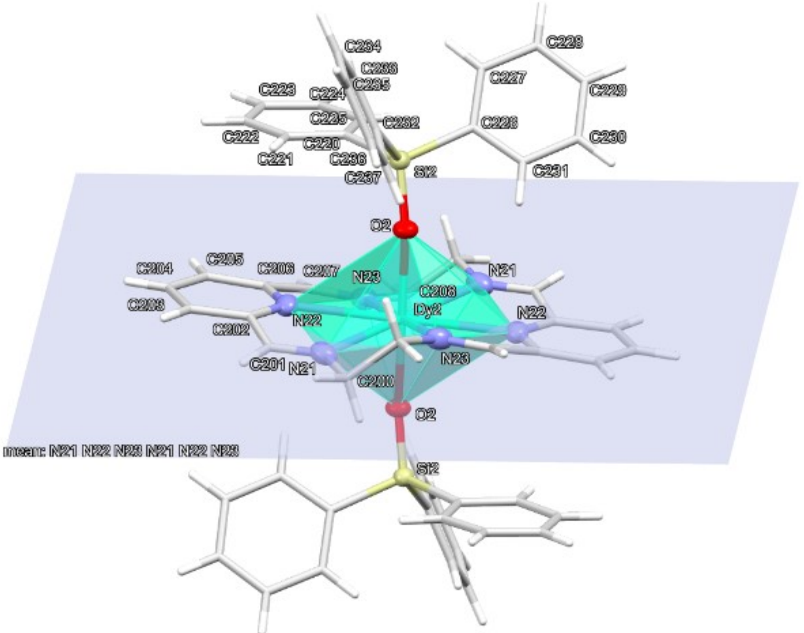

Figure S2. Balls and sticks diagram for the cation $[Dy(L^{N6en})(OSiPh_3)_2]^+$ in the $\{[Dy(L^{N6en})(OSiPh_3)_2](BPh_4)\}$ complex **1b**, showing Dy2 as a polyhedron. Labels for atoms not corresponding to the asymmetric unit have been mostly omitted for clarity.

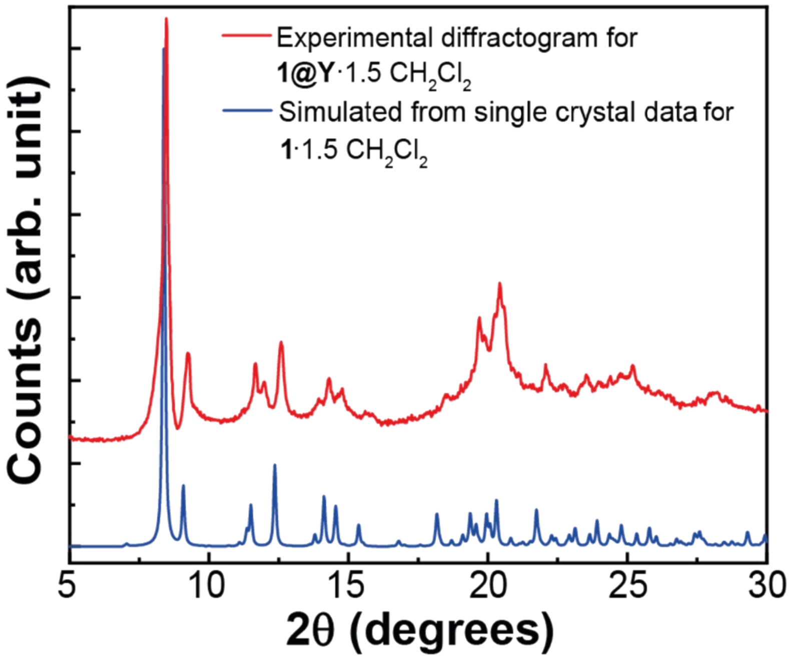

Figure S3. Comparative powder X-ray diffractograms for **1@**Y·1.5CH_2Cl_2 (red) and the simulation from **1**·1.5CH_2Cl_2 diffraction data (blue).

3. Magnetic characterization and SMM behaviour

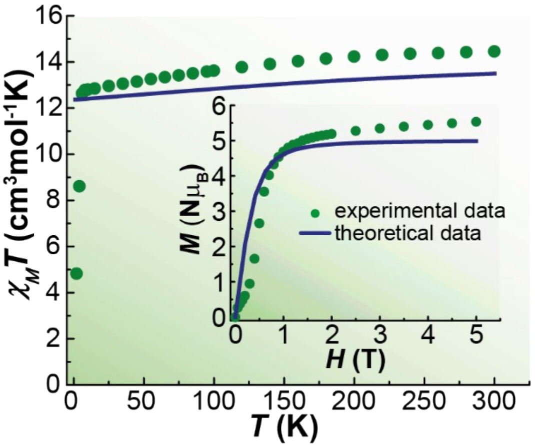

Figure S4. $\chi_M T$ vs T graph for **1**·1.5CH$_2$Cl$_2$. Inset: $M/N\mu_B$ vs H at 2 K. The blue lines represent the theoretical data obtained from *ab initio* calculations.

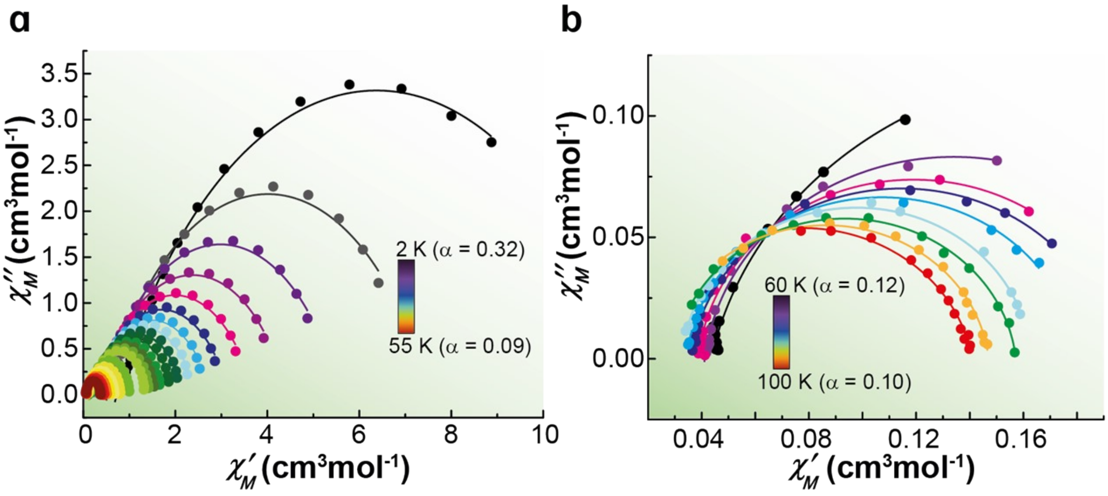

Figure S5. Cole-Cole graphs for **1**·1.5CH$_2$Cl$_2$ at H_{dc} = 0 in the range (a) 2-55 K and (b) 60-100 K. T Solid lines are fits to the data.

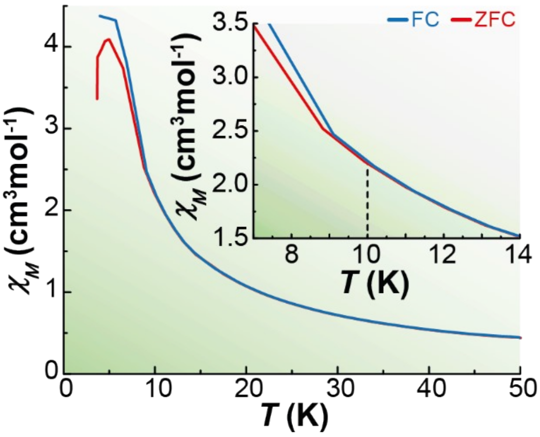

Figure S6. FC and ZFC magnetic susceptibility of **1**·1.5CH$_2$Cl$_2$ under an applied magnetic field of 2000 Oe (warm mode, 2 Kmin^{-1}).

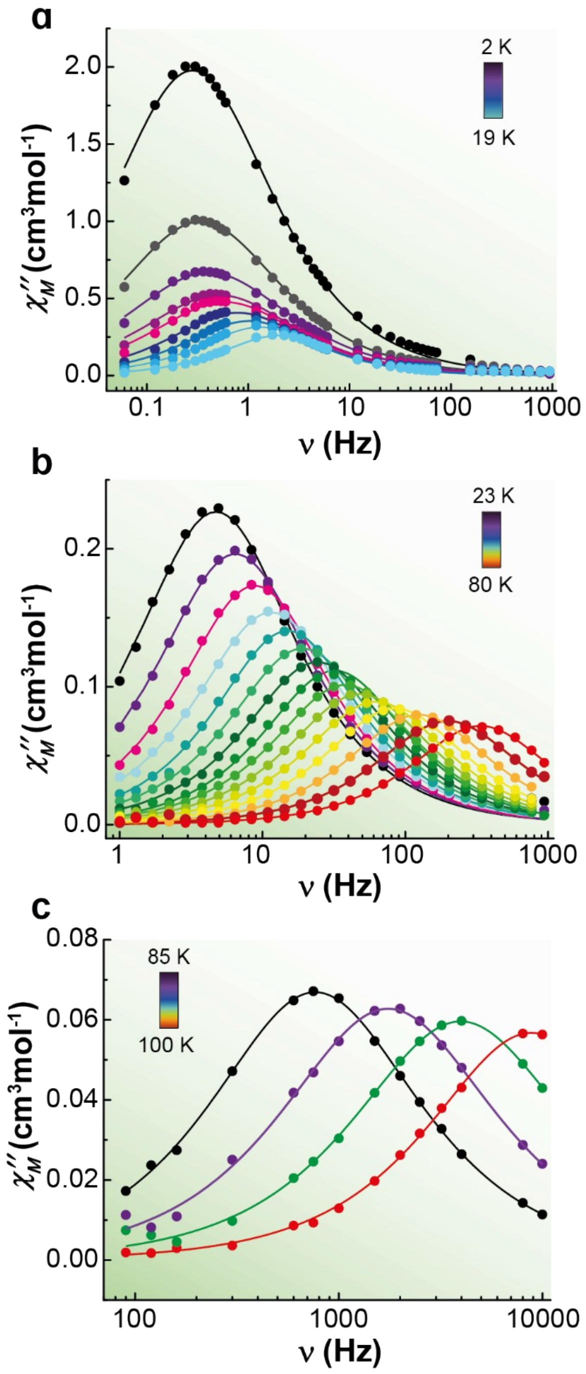

Figure S7. Frequency dependence of χ''_M for **1@Y**·1.5CH$_2$Cl$_2$ at H_{dc} = 0 at frequencies ranging from: (a) 0.1 to 1000 Hz between 2 and 19 K; (b) 1 to 1000 Hz between 23 and 80 K; (c) 50 to 10000 Hz between 85 and 100 K. Solid lines are fits to the data.

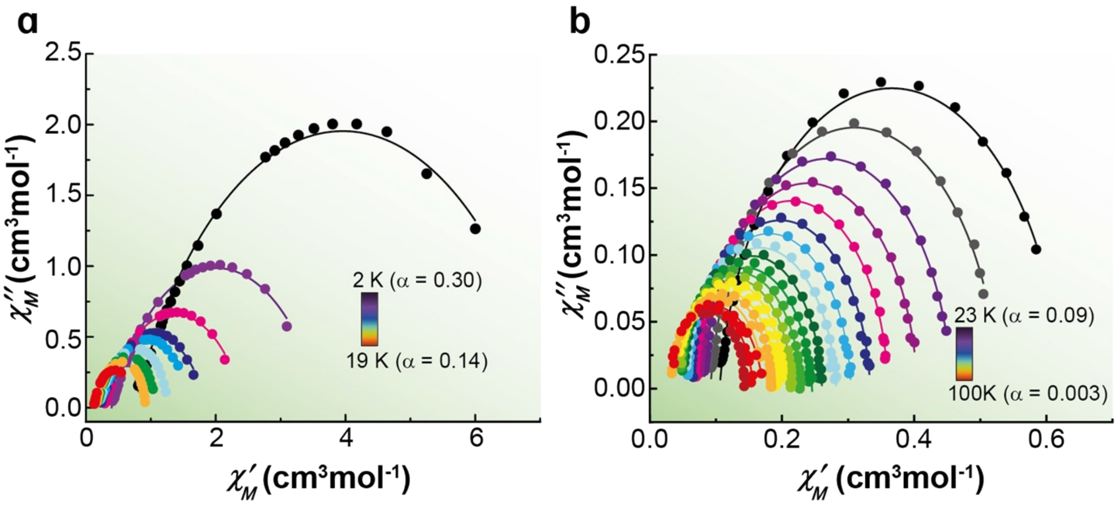

Figure S8. Cole-Cole graphs for **1@Y**·1.5CH$_2$Cl$_2$ at H_{dc} = 0 in the range (a) 2-19 K and (b) 23-100 K.

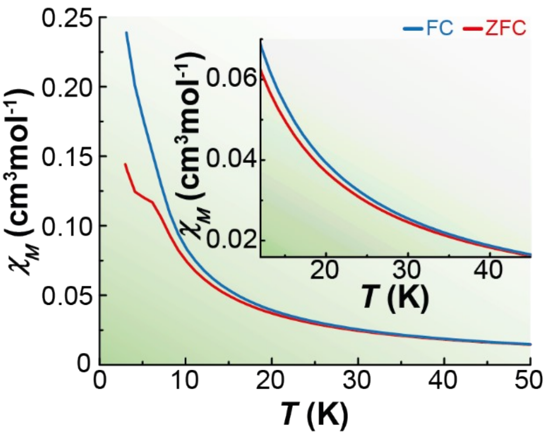

Figure S9. FC and ZFC magnetic susceptibility of **1@Y**·1.5CH$_2$Cl$_2$ under an applied magnetic field of 2000 Oe (warm mode, 2 Kmin^{-1}). Inset: expansion between 12 and 42 K.

Table S5. Generalized Debye model fitting parameters for **1**·1.5CH_2Cl_2 and **1@Y**·1.5CH_2Cl_2.

Compounds	***T*/K**	**χ_S/(cm^{3}mol^{-1})**	**χ_T/(cm^{3}mol^{-1})**	**τ/s**	**α**
1·1.5CH_2Cl_2	2	0.68	8.87	0.23945	0.32
	3	0.50	6.42	0.221875	0.29
	4	0.39	4.87	0.219109	0.28
	5	0.32	3.92	0.203219	0.28
	6	0.33	3.31	0.1984	0.28
	7	0.25	2.86	0.1773	0.28
	8	0.22	2.52	0.1585	0.28
	9	0.19	2.26	0.1412	0.27
	10	0.18	2.04	0.1263	0.26
	11	0.16	1.85	0.112	0.26
	12	0.15	1.65	0.10484	0.24
	13	0.14	1.54	0.097237	0.24
	14	0.13	1.41	0.087675	0.22
	15	0.12	1.32	0.075895	0.22
	20	0.11	1.00	0.048159	0.16
	25	0.10	0.79	0.032133	0.12
	30	0.09	0.68	0.02058	0.08
	35	0.07	0.57	0.01456	0.08
	40	0.07	0.50	0.01051	0.08
	45	0.07	0.45	0.007749	0.07
	50	0.06	0.41	0.005824	0.09
	55	0.05	0.38	0.004318	0.09
	60	0.05	0.35	0.003057	0.12
	65	0.04	0.15	0.001995	0.07
	70	0.04	0.16	0.001575	0.05
	75	0.04	0.17	9.768E-4	0.07
	80	0.03	0.17	4.932E-4	0.06
	85	0.03	0.16	2.104E-4	0.03
	90	0.04	0.16	8.877999E-5	0.06
	95	0.05	0.15	3.916E-5	0.06
	100	0.07	0.14	1.798E-5	0.10
1@Y·1.5CH_2Cl_2	2	0.81	6.00	0.5705	0.30
	4	0.39	3.09	0.4741	0.30
	5.5	0.29	2.14	0.3914	0.30
	7.6	0.24	1.66	0.3079	0.29
	9.5	0.22	1.42	0.268	0.29
	11.0	0.20	1.23	0.2021	0.21
	13	0.17	1.03	0.1561	0.19
	15	0.15	0.91	0.121	0.14
	19	0.13	0.54	0.07931	0.14
	23	0.11	0.58	0.03375	0.09
	27	0.09	0.50	0.02468	0.07
	31	0.08	0.45	0.01801	0.06
	35	0.07	0.40	0.01382	0.05
	39	0.07	0.36	0.0106	0.03
	43	0.07	0.33	0.008332	0.05
	47.5	0.06	0.30	0.00657	0.04
	51.5	0.06	0.28	0.005237	0.06
	55.5	0.05	0.26	0.00419	0.04
	60	0.05	0.24	0.003311	0.07
	63.7	0.05	0.23	0.002553	0.04

	67.8	0.05	0.21	0.001876	0.03
	71.9	0.05	0.20	0.001279	0.08
	75.9	0.05	0.19	7.992E-4	0.06
	80	0.04	0.18	4.724E-4	0.03
	85	0.03	0.17	2.079E-4	0.02
	90	0.03	0.17	9.123E-5	0.11
	95	0.05	0.15	4.02E-5	0.06
	100	0.07	0.14	1.854E-5	0.03

4. Theoretical calculations

Computational Details

The experimental coordinates obtained from the cif file were employed for the theoretical calculations. There are two crystallographically different halves of the cationic complex $[Dy(L^{N6en})(OSiPh_3)_2]^+$, giving to two whole complex molecules, which are called **1a** and **1b**. In the case of the cation **1b** some atoms are disordered on two sites with occupations close to 0.5. So three different cations have been calculated, **1a** and the two units for **1b**, **1b_1** and **1b_2**, which differ on the position of two nitrogen atoms and the ethylene chain, see Figure S10. The electronic structure and magnetic properties have been computed with the ORCA 5.0.3 quantum chemistry program package,[11-13] using state averaged complete active space self-consistent field calculations (SA-CASSCF)[14] with an active space including the nine *f* electrons in the seven 4*f* orbitals (9,7). Within this active space, 21 sextets states, 128 quadruplets and 98 doublets have been computed. Spin-orbit effects were included using the quasi-degenerate perturbation theory (QDPT).[15] The def2-TZVPP basis set was employed, including the corresponding auxiliary basis sets for correlation and Coulomb fitting for all the atoms.[16-20] The SINGLE_ANISO approach was also employed for the magnetic properties and the transition probabilities between the states to compute the *ab initio* blocking barrier.[21]

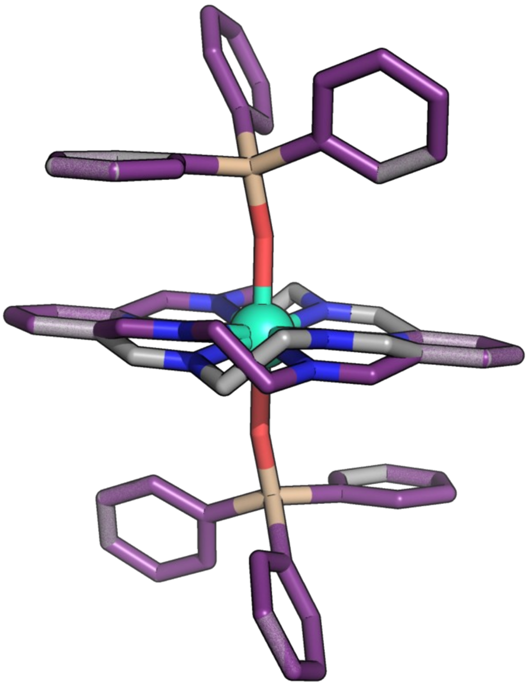

Figure S10. Superposition of **1b_1** (C atoms in grey) and **1b_2** (C atoms in purple) to highlight the differences between them. Dysprosium, silicon, oxygen and nitrogen are represented in cyan, light brown, red and blue, respectively. Hydrogen atoms are omitted for clarity.

Table S6. Information of the eight low lying KDs calculated at CASSCF level. Relative energies (in cm^{-1}), components of the *g*-tensor, and tilting angle (θ) of the g_{zz} component of the corresponding excited state KD with respect to the ground state KD for **1b_1**.

Energy (cm^{-1})	g_{xx}	g_{yy}	g_{zz}	θ (°)
0.0	0.00059	0.00096	19.872	
489.6	0.101	0.112	16.947	2.470
868.7	0.508	0.633	13.757	6.865
1071.6	4.567	5.932	9.845	70.982
1129.5	1.463	4.373	11.804	85.380
1195.5	2.212	5.830	11.241	85.623
1282.6	0.440	1.539	16.058	89.478
1360.0	0.655	2.610	16.370	79.313

Table S7. Information of the eight low lying KDs calculated at CASSCF level. Relative energies (in cm^{-1}), components of the *g*-tensor, and tilting angle (θ) of the g_{zz} component of the corresponding excited state KD with respect to the ground state KD for **1b_2**.

Energy (cm^{-1})	g_{xx}	g_{yy}	g_{zz}	θ (°)
0.0	0.00007	0.00016	19.884	
502.6	0.052	0.053	16.995	5.769
917.1	0.124	0.171	14.110	8.553
1185.8	1.347	1.442	10.491	21.215
1282.4	1.708	8.483	11.203	81.891
1314.6	0.149	4.370	12.344	88.983
1377.0	1.487	1.787	7.754	73.706
1449.0	0.668	5.691	14.128	70.342

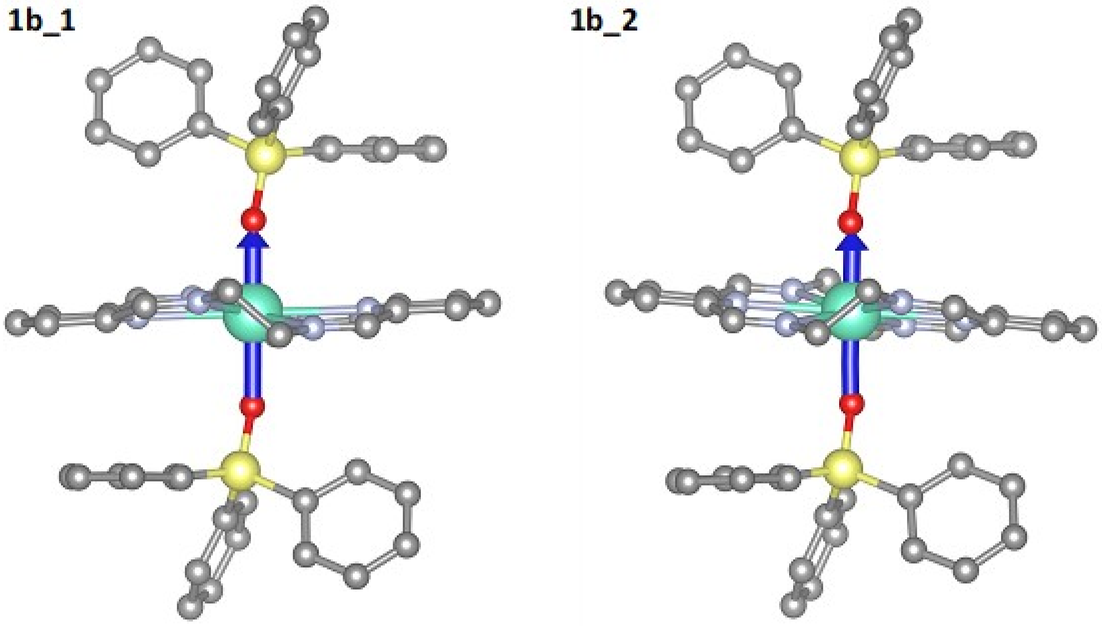

Figure S11. CASSCF calculated orientation of the main magnetic axis of the ground Kramers doublet of **1b_1** (left) and **1b_2** (right). Dysprosium, silicon, oxygen, nitrogen and carbon are represented in cyan, yellow, red, light blue and grey, respectively. Hydrogen atoms are omitted for clarity.

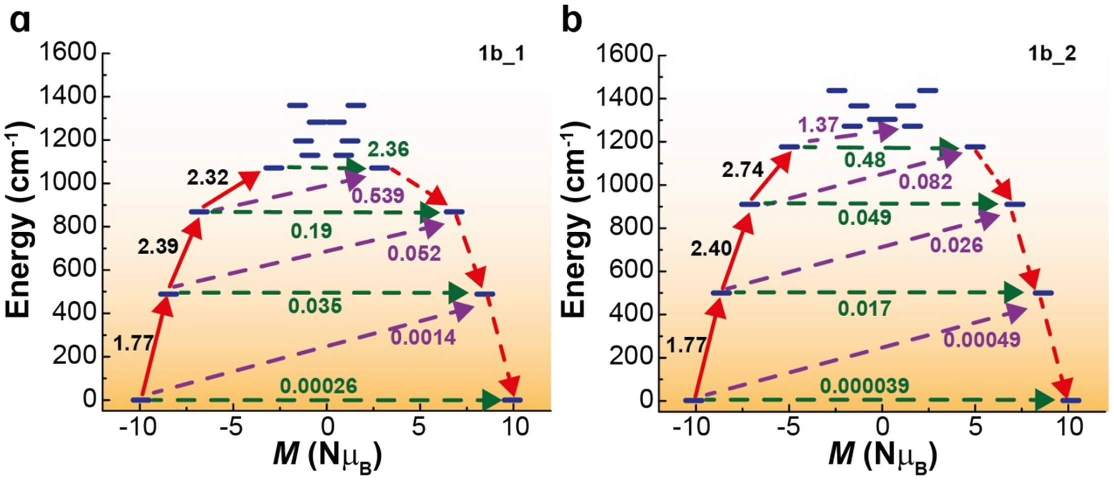

Figure S12. States energies as a function of their average magnetic moment, *M*, along the main anisotropy axis for (a) **1b_1** and (b) **1b_2** obtained with SINGLE_ANISO. The dashed green arrows correspond to the quantum tunnelling mechanism of ground or excited states, and dashed purple arrow shows the hypothetical Orbach relaxation process. The solid red arrows indicate the transition between the ground and excited Kramers doublets, and the dashed red arrows the excitation pathway to the ground state with the reversed spin. The values close to the arrows indicate the matrix elements of the transition magnetic moments (above 0.1 an efficient spin relaxation mechanism is expected).

5. Photoluminescence data

A custom MATLAB® routine was developed to determine the integrated area of the emission spectra of the two compounds. First, the baseline was subtracted and then the spectra were converted from wavelength to energy scale, ensuring consistency in evaluating emission intensities across the spectral range, using:

$$E = \frac{10^7}{\lambda} \tag{S1}$$

where E is the energy (in cm^{-1}) and λ is the corresponding wavelength (in nm). However, the signal value recorded from the spectrometer is a signal per unit wavelength. Due to the inverse relationship between wavelength and energy, the interval $d\lambda$ in the wavelength spectrum has different dE sizes across the entire energy spectrum. Therefore, based on energy conservation, the intensity signal also needs to be corrected as follows:

$$f(E) = f(\lambda)\frac{d\lambda}{dE} = f(\lambda)\frac{d}{dE}\left(\frac{10^7}{E}\right) = - f(\lambda)\frac{10^7}{E^2} \tag{S2}$$

where $f(E)$ and $f(\lambda)$ are the intensities as a function of energy and wavelength, respectively. This is also known as Jacobian transformation and the minus sign here can be ignored as it merely shows the opposite directions of integration in wavelength and energy.[22, 23] The wavelength-to-energy conversion is particularly important where multiple peaks are present or when the emission band spans a broad spectral range.

To quantitatively analyse the emitter populations and understand the cause of the linewidth, the Jacobian-corrected spectra should be further processed to extract information about the emitter populations from their relative peak areas. The process involves converting the spectra into specific line shapes by factoring out the E^3 dependence of spontaneous emission as:[24-26]

$$\frac{f(E)}{E^3} = - f(\lambda)\frac{10^7}{E^5} \tag{S3}$$

For **1**·1.5CH$_2$Cl$_2$, the integrated areas of the intra-4f transitions, which overlap with the broadband emission (Fig. S14a), were determined by first subtracting a straight baseline and subsequently performing numerical integration, between 460 and 505 nm, for $^4F_{9/2} \rightarrow {}^6H_{15/2}$, and 550 and 630 nm, for $^4F_{9/2} \rightarrow {}^6H_{13/2}$. The area of the broadband emission was obtained by subtracting the area of these two intra-4f transitions from the total integrated area (between 380 and 650 nm).

For **1@Y**·1.5CH$_2$Cl$_2$, the broadband emission was deconvoluted into two Gaussian components using MATLAB®. The routine extracted the integrated areas of the two Gaussian functions, as well as their respective full width at half maximum (FWHM) and peak energy values. These parameters are presented in Table S10. The deconvolution process, including the fit of the Gaussian components, is illustrated in Figure S15.

The relative thermal sensitivity (S_r) of **1**·1.5CH$_2$Cl$_2$ and **1@Y**·1.5CH$_2$Cl$_2$ were estimated by:[27, 28]

$$S_r = \frac{1}{\Delta}\left|\frac{\partial \Delta}{\partial T}\right| \tag{S4}$$

where Δ is the thermometric parameter (Δ_1, **1**·1.5CH$_2$Cl$_2$ and Δ_2, **1@Y**·1.5CH$_2$Cl$_2$, defined in the main text), and T the temperature (measured by the Si diode).

The temperature uncertainty (δT), which quantifies the temperature resolution:[27, 28]

$$\delta T = \frac{1}{S_r}\frac{\delta \Delta}{\Delta} \tag{S5}$$

being $\delta\Delta/\Delta$ the relative uncertainty in Δ estimated through:

$$\delta\Delta_1 = \Delta_1\sqrt{\left(\frac{\delta I_1}{I_1}\right)^2+\left(\frac{\delta I_2}{I_2}\right)^2+\left(\frac{\delta I_3}{I_3}\right)^2} \tag{S6}$$

$$\delta\Delta_2 = \Delta_2\sqrt{\left(\frac{\delta A_1}{A_1}\right)^2+\left(\frac{\delta A_2}{A_2}\right)^2} \tag{S7}$$

where $\delta I_i/I_i$ (i = 1, 2, 3) is calculated dividing the readout fluctuations of the baseline by the maximum value of each intensity, *i.e.*, I_1, I_2 and I_3. As the integrated areas are calculated from the same emission spectra then $\delta I_1 = \delta I_2 = \delta I_3 = \delta I$; and $\delta A_i/A_i$ (i = 1, 2) is calculated by dividing the error associated with the area by the area, both parameters obtained from the deconvolution process.

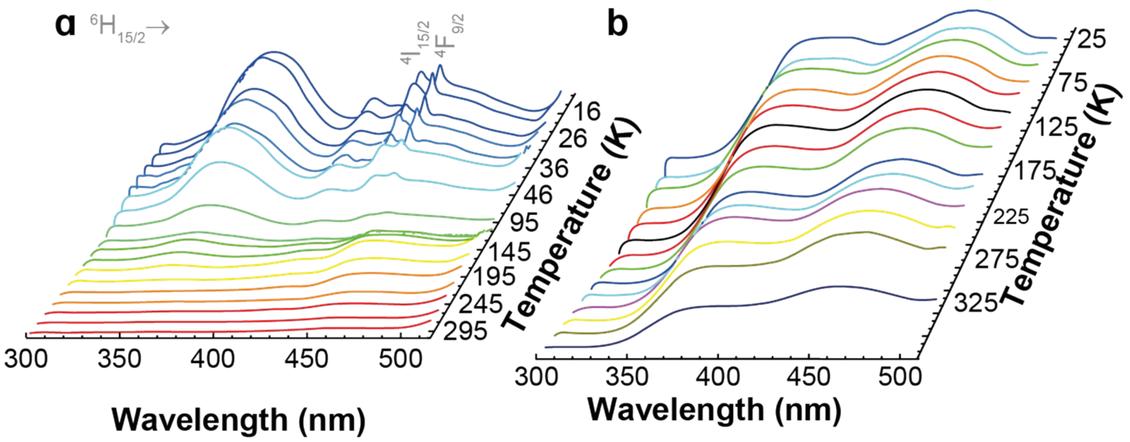

Figure S13. (a) Excitation spectra for **1**·1.5CH$_2$Cl$_2$ in the 13-295 K temperature range, monitoring the $^4F_{9/2} \rightarrow {}^6H_{13/2}$ transition at 590 nm (Figure S13). (b) Excitation spectra for **1@Y**·1.5CH$_2$Cl$_2$ in the 13-325 K temperature range, monitoring the broad band at 575 nm (Figure 6).

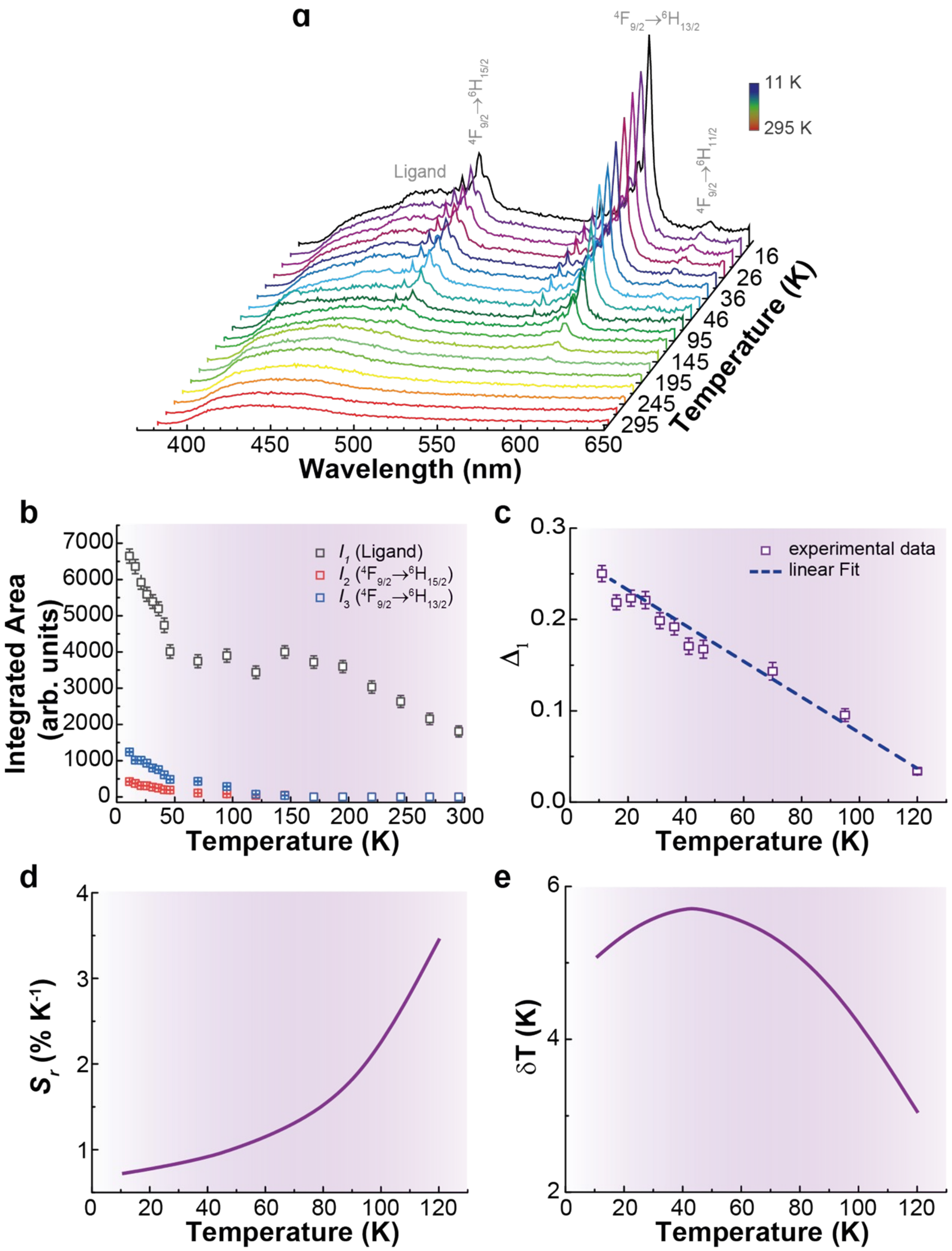

Figure S14. (a) Temperature-dependent (13-295 K) emission spectra of **1**·1.5CH$_2$Cl$_2$ excited at 364- nm. (b) Temperature dependence of the integrated emission area for compound **1**·1.5CH$_2$Cl$_2$. (c) Temperature dependence of the thermometric parameter (Δ_1) for **1**·1.5CH$_2$Cl$_2$. The line represents the best linear fit ($r^2 > 0.99$) to the experimental data (fit details provided in Table S8). (e) Temperature dependence of S_r for **1**·1.5CH$_2$Cl$_2$. (f) Temperature dependence of δT for **1**·1.5CH$_2$Cl$_2$.

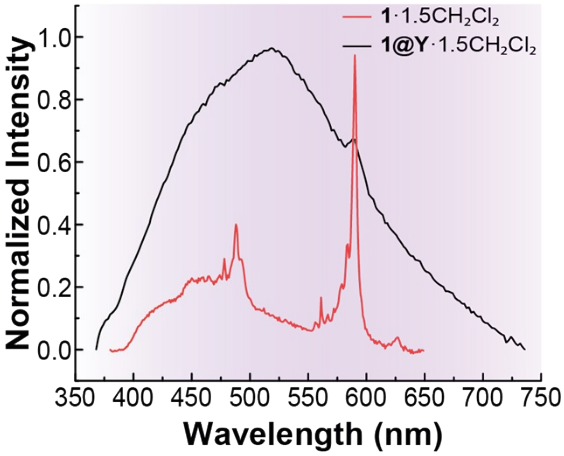

Figure S15. Emission spectra of **1**·1.5CH$_2$Cl$_2$ (red) and **1@Y**·1.5CH$_2$Cl$_2$ (black) recorded at 13 K excited at 364 nm.

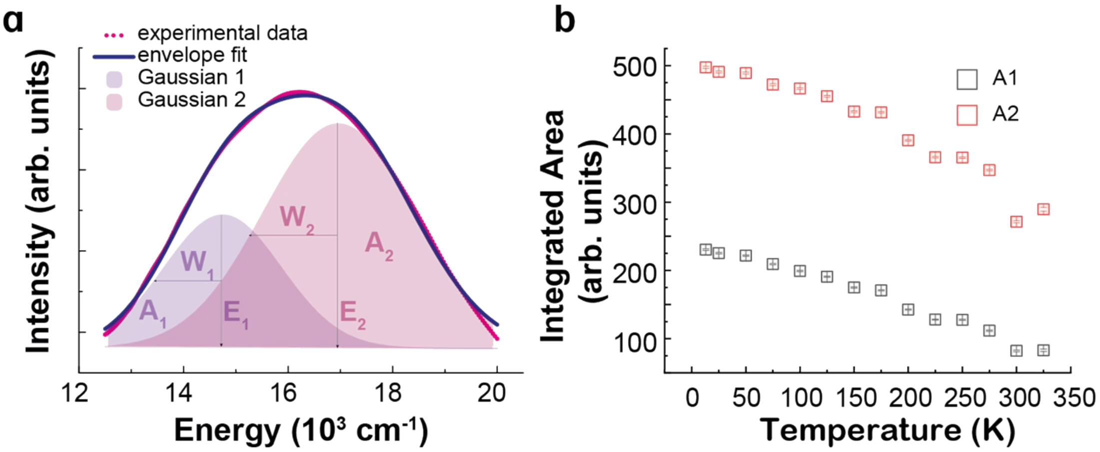

Figure S16. (a) Illustration of the deconvolution process for compound **1@Y**·1.5CH$_2$Cl$_2$ at 13 K, performed using OriginLab®. The Gaussian components are labelled as 1 for lower energy and 2 for higher energy. (b) Temperature dependence of the integrated area (A_i) for the Gaussian components i = 1, 2.

Table S8. Value of the intercept (a), slope (b) of the linear fit and r^2 for **1**·1.5CH$_2$Cl$_2$ and **1@Y**·1.5CH$_2$Cl$_2$.

Sample	Thermometric Parameter	Variable	Value
1·1.5CH$_2$Cl$_2$	Δ_1	a	0.255±0.01
		b	(−1.71±0.08)×10^{-3}
		r^2	0.98
1@Y·1.5CH$_2$Cl$_2$	Δ_2	a	0.48±0.04
		b	(−5.4±0.3)×10^{-4}
		r^2	0.98

Table S9. Calculated excitation energies (singlets and triplets in nm) of the ligands and BPh$_4^-$ counterion using the experimental structure in the complex **1** using the STEOM-DLPNO-CCSD method[12, 29-34] with Orca 5.0.3 code[11-13] (def2-TZVP basis set and auxiliary def2-TZVP/C and def2/J basis sets).[17, 18] In bold are highlighted the excited singlet states with higher oscillation strength.

ligand	L^{N6en}		$^-$OSiPh$_3$		BPh$_4^-$	
	Singlets	Triplets	Singlets	Triplets	Singlets	Triplets
	283	423	**309**	371	261	420
	275	411	297	358	260	387
	260	348	270	358	**257**	340
	253	335	268	280	256	311

Table S10. Fitting parameters of the deconvolution of the emission spectrum of **1@Y**·1.5CH_2Cl_2 recorded at distinct temperatures using two Gaussian components. The amplitudes (A_1 and A_2), the mean peak energies (E_1 and E_2), the widths (W_1 and W_2) of peaks 1 and 2, and the coefficient of determination (r^2) were obtained with OriginLab® software.

Temperature (K)	Fitting parameter	Value ($\times 10^2$)	r^2
13	A_1	230±1	0.998
	A_2	497±2	
	E_1	147.±9	
	E_2	170±5	
	W_1	26.4±0.1	
	W_2	33.9±0.1	
25	A_1	225±1	0.998
	A_2	491±1	
	E_1	147.47±9	
	E_2	170±5	
	W_1	26.3±0.1	
	W_2	33.8±0.1	
50	A_1	222±1	0.998
	A_2	489±1	
	E_1	150±9	
	E_2	170±5	
	W_1	26.5±0.1	
	W_2	33.9±0.1	
75	A_1	209±1	0.998
	A_2	472±2	
	E_1	147±9	
	E_2	170±5	
	W_1	26.8±0.1	
	W_2	34.1±0.1	
100	A_1	199.1±0.9	0.998
	A_2	466±1	
	E_1	147±9	
	E_2	170±5	
	W_1	26.4±0.1	
	W_2	34.2±0.1	
125	A_1	190.8±0.9	0.998
	A_2	455±1	
	E_1	147±9	
	E_2	169.58±5	
	W_1	26.7±0.1	
	W_2	34.5±0.1	
150	A_1	175.0±0.8	0.998
	A_2	433±1	
	E_1	147±9	
	E_2	170±5	
	W_1	27.0±0.1	
	W_2	34.9±0.1	
175	A_1	170.7±0.7	0.999
	A_2	431±1	
	E_1	147±9	
	E_2	170±5	
	W_1	29.4±0.1	

	W_2	37.1±0.1	
200	A_1	142.7±0.8	0.998
	A_2	391±1	
	E_1	147±9	
	E_2	170±5	
	W_1	30.6±0.1	
	W_2	37.9±0.1	
225	A_1	128.0±0.7	0.998
	A_2	366±1	
	E_1	147±9	
	E_2	170±5	
	W_1	27.6±0.1	
	W_2	36.0±0.1	
250	A_1	127.6±0.8	0.998
	A_2	365±1	
	E_1	147±9	
	E_2	170±5	
	W_1	31.5±0.1	
	W_2	38.4±0.1	
275	A_1	111.7±0.8	0.998
	A_2	347±1	
	E_1	147±9	
	E_2	170±5	
	W_1	32.0±0.2	
	W_2	39.1±0.1	
300	A_1	82±1	0.997
	A_2	271±1	
	E_1	147±9	
	E_2	170±5	
	W_1	28.2±0.7	
	W_2	37.1±0.5	
325	A_1	83±1	0.996
	A_2	290±2	
	E_1	147±9	
	E_2	170±5	
	W_1	27.4±0.4	
	W_2	35.0±0.2	

7. References

1 J. Corredoira-Vázquez, C. González-Barreira, A. M. García-Deibe, J. Sanmartín-Matalobos, M. A. Hernández-Rodríguez, C. D. S. Brites, L. D. Carlos and M. Fondo, Harnessing ligand design to develop primary and self-calibrated luminescent thermometers with field-induced single ion magnet behaviour in Dy^{3+} complexes, *Inorg. Chem. Front.*, 2024, **11**, 1087-1098.

2 G. M. Sheldrick, SADABS, Program for Empirical Absorption Correction of Area Detector Data, 1996.

3 G. Sheldrick, SHELXT - Integrated space-group and crystal-structure determination, *Acta Crystallogr., Sect. A: Found. Adv.*, 2015, **71**, 3-8.

4 G. M. Sheldrick, Crystal structure refinement with SHELXL, *Acta crystallogr., C Struct. chem.*, 2015, **71**, 3-8.

5 Z. Zhu, C. Zhao, Q. Zhou, S. Liu, X.-L. Li, A. Mansikkamäki and J. Tang, Air-Stable Dy(III)-Macrocycle Enantiomers: From Chiral to Polar Space Group, *CCS Chemistry*, 2022, **4**, 3762-3771.

6 S. Liu, Y. Gil, C. Zhao, J. Wu, Z. Zhu, X.-L. Li, D. Aravena and J. Tang, A conjugated Schiff-base macrocycle weakens the transverse crystal field of air-stable dysprosium single-molecule magnets, *Inorg. Chem. Front.*, 2022, **9**, 4982-4989.

7 Z. Zhu, C. Zhao, T. Feng, X. Liu, X. Ying, X.-L. Li, Y.-Q. Zhang and J. Tang, Air-stable chiral single-molecule magnets with record anisotropy barrier exceeding 1800 K, *J. Am. Chem. Soc.*, 2021, **143**, 10077-10082.

8 A. B. Canaj, S. Dey, E. R. Martí, C. Wilson, G. Rajaraman and M. Murrie, Insight into D_{6h} symmetry: targeting strong axiality in stable dysprosium(III) hexagonal bipyramidal single-ion magnets, *Angew. Chem. Int. Ed.*, 2019, **58**, 14146-14151.

9 S. Jia, X. Zhu, B. Yin, Y. Dong, A. Sun and D.-f. Li, Macrocyclic hexagonal bipyramidal Dy(III)-based single-molecule magnets with a D_{6h} symmetry, *Cryst. Growth Des,*, 2023, **23**, 6967-6973.

10 J. Corredoira-Vázquez, C. González-Barreira, P. Oreiro-Martínez, A. M. García-Deibe, J. Sanmartín-Matalobos and M. Fondo, Synthesis and applications of lanthanoid complexes of pentadentate and hexadentate N_5 and N_6 macrocycles: A review, *J. Rare Earths*, 2024, **42**, 1-15.

11 F. Neese, Software update: the ORCA program system, version 4.0, *WIREs Comput. Mol. Sci.*, 2018, **8**, e1327.

12 F. Neese, F. Wennmohs, U. Becker and C. Riplinger, The ORCA quantum chemistry program package, *J. Chem. Phys.*, 2020, **152**, 224108.

13 F. Neese, Software update: The ORCA program system—Version 5.0, *WIREs Comput. Mol. Sci.*, 2022, **12**, e1606.

14 P.-Å. Malmqvist and B. O. Roos, The CASSCF state interaction method, *Chem. Phys. Lett.*, 1989, **155**, 189-194.

15 D. Ganyushin and F. Neese, First-principles calculations of zero-field splitting parameters, *J. Chem. Phys.*, 2006, **125**, 024103.

16 M. Dolg, H. Stoll and H. Preuss, A combination of quasirelativistic pseudopotential and ligand field calculations for lanthanoid compounds, *Theor. Chim. Acta*, 1993, **85**, 441-450.

17 F. Weigend and R. Ahlrichs, Balanced basis sets of split valence, triple zeta valence and quadruple zeta valence quality for H to Rn: design and assessment of accuracy, *Phys. Chem. Chem. Phys.*, 2005, **7**, 3297-3305.

18 F. Weigend, Accurate Coulomb-fitting basis sets for H to Rn, *Phys. Chem. Chem. Phys.*, 2006, **8**, 1057-1065.

19 A. Hellweg, C. Hättig, S. Höfener and W. Klopper, Optimized accurate auxiliary basis sets for RI-MP2 and RI-CC2 calculations for the atoms Rb to Rn, *Theor. Chem. Acc.*, 2007, **117**, 587-597.

20 J. Chmela and M. E. Harding, Optimized auxiliary basis sets for density fitted post-Hartree–Fock calculations of lanthanide containing molecules, *Mol. Phys.*, 2018, **116**, 1523-1538.

21 L. F. Chibotaru and L. Ungur, Ab initio calculation of anisotropic magnetic properties of complexes. I. Unique definition of pseudospin Hamiltonians and their derivation, *J. Chem. Phys.*, 2012, **137**.

22 J. Mooney and P. Kambhampati, Get the basics right: Jacobian conversion of wavelength and energy scales for quantitative analysis of emission spectra, *J. Phys. Chem. Lett.*, 2013, **4**, 3316-3318.

23 J. Mooney and P. Kambhampati, Correction to “Get the basics right: Jacobian conversion of wavelength and energy scales for quantitative analysis of emission spectra”, *J. Phys. Chem. Lett.*, 2014, **5**, 3497-3497.

24 J. Mooney, M. M. Krause, J. I. Saari and P. Kambhampati, A microscopic picture of surface charge trapping in semiconductor nanocrystals, *J. Chem. Phys.*, 2013, **138**, 204705.

25 M. M. Krause, J. Mooney and P. Kambhampati, Chemical and thermodynamic control of the surface of semiconductor nanocrystals for designer white light emitters, *ACS Nano*, 2013, **7**, 5922-5929.

26 A. B. Myers, Relating absorption, emission, and resonance Raman spectra with electron transfer rates in photoinduced charge transfer systems: promises and pitfalls, *Chem. Phys.*, 1994, **180**, 215-230.

27 C. D. S. Brites, P. P. Lima, N. J. O. Silva, A. Millán, V. S. Amaral, F. Palacio and L. D. Carlos, Thermometry at the nanoscale, *Nanoscale*, 2012, **4**, 4799-4829.

28 C. D. S. Brites, A. Millán and L. D. Carlos, in *Handbook on the Physics and Chemistry of Rare Earths*, eds. J.-C. G. Bünzli and V. K. Pecharsky, Elsevier Science, B. V., Amsterdam, 2016, vol. 49, ch. 281, pp. 339-427.

29 A. K. Dutta, M. Nooijen, F. Neese and R. Izsák, Exploring the accuracy of a low scaling similarity transformed equation of motion method for vertical excitation energies, *J. Chem. Theory Comput.*, 2017, **14**, 72-91.

30 A. K. Dutta, M. Nooijen, F. Neese and R. Izsák, Automatic active space selection for the similarity transformed equations of motion coupled cluster method, *J. Chem. Phys.*, 2017, **146**, 074103.

31 A. K. Dutta, F. Neese and R. Izsák, Towards a pair natural orbital coupled cluster method for excited states, *J. Chem. Phys.*, 2016, **145**, 034102.

32 M. Nooijen and R. J. Bartlett, Similarity transformed equation-of-motion coupled-cluster theory: details, examples, and comparisons, *J. Chem. Phys.*, 1997, **107**, 6812-6830.

33 M. Nooijen and R. J. Bartlett, A new method for excited states: similarity transformed equation-of-motion coupled-cluster theory, *J. Chem. Phys.*, 1997, **106**, 6441-6448.

34 J. Sous, P. Goel and M. Nooijen, Similarity transformed equation of motion coupled cluster theory revisited: a benchmark study of valence excited states, *Mol. Phys.*, 2013, **112**, 616-638.